Film Cooling Modeling in a Turbine Working under the Unsteady Exhaust Flow of Pulsed Detonation Combustion

*energies*

MDPI

*Article*

# Film Cooling Modeling in a Turbine Working under the Unsteady Exhaust Flow of Pulsed Detonation Combustion

**Gokkul Raj Varatharajulu Purgunan [1,*], Majid Asli [2], Teodosio Nacci [3], Daniela Anna Misul [3], Simone Salvadori [3] and Panagiotis Stathopoulos [4]**

[1] Institute of Fluid Mechanics and Technical Acoustics, Technische Universität Berlin, 10623 Berlin, Germany
[2] Chair of Aeroengine Design, Brandenburg University of Technology Cottbus-Senftenberg, 03046 Cottbus, Germany; asli@b-tu.de
[3] Department of Energy (DENERG), Politecnico di Torino, 10129 Turin, Italy; teodosio.nacci@polito.it (T.N.); simone.salvadori@polito.it (S.S.)
[4] Institute of Low Carbon Industrial Processes, German Aerospace Center (DLR), 51147 Cottbus, Germany
* Correspondence: gokkul.raj.varatharajulu.purgunan@tu-berlin.de

**Abstract:** Pressure gain combustors (PGCs) have demonstrated significant advantages over conventional combustors in gas turbine engines by increasing the thermal efficiency and reducing the pollution emission level. PGCs use shock waves to transfer energy which contributes to the increase in outlet total pressure. One of the major obstacles in the actual implementation of PGCs in the gas turbine cycle is the exploitation of the highly unsteady flow of the combustor outlet with the downstream turbine. Because of the higher outlet temperature from the PGCs, the turbine blade cooling becomes essential. Due to the highly fluctuating unsteady flow of PGCs, 3D CFD simulation of turbines becomes very expensive. In this work, an alternative approach of using a 1D unsteady Euler model for the turbine is proposed. One of the novel aspects of this paper is to implement the turbine blade cooling in the unsteady 1D Euler model. The main parameters required for the turbine blade cooling are the cooling air mass flow rate, temperature, and pressure. Due to the introduction of coolant flow, the blades are no longer adiabatic and the mass flow rate across the turbine is not constant. Comparing the 1D Euler results against zero-dimensional calculation and 3D CFD approach showed a very good match for both steady and unsteady simulations confirming the applicability of the 1D method.

**Keywords:** pressure gain combustor; turbomachinery; unsteady interaction; film cooling; Euler equations; computational fluid dynamics



**Citation:** Varatharajulu Purgunan, G.R.; Asli, M.; Nacci, T.; Misul, D.A.; Salvadori, S.; Stathopoulos, P. Film Cooling Modeling in a Turbine Working under the Unsteady Exhaust Flow of Pulsed Detonation Combustion. *Energies* **2024**, *17*, 1312. https://doi.org/10.3390/en17061312

Academic Editor: Francesco Minichiello

Received: 8 February 2024
Revised: 27 February 2024
Accepted: 5 March 2024
Published: 8 March 2024



## 1. Introduction

As global warming and pollutant emissions are the primary concerns in today's world, numerous studies and a lot of research are being conducted to reduce emissions. The transportation system is a major source of pollution and greenhouse gas emissions. Meanwhile, the use of the air transportation system is increasing on a yearly basis [1]. The International Civil Aviation Organization predicts an increase by 2.2 times in the next twenty years. Thus, reduction in emissions from air transportation is vital. Gas turbine engines are already approaching the efficiency limit imposed by the underlying thermodynamic cycle. One of the approaches to achieve an increase in propulsive efficiency is to modify the existing gas turbine cycles with new ideas. In the recent years, pressure gain combustors have attained a lot of attention for propulsive applications. Researchers provide conclusive results that the PGCs can improve the thermal efficiency of the gas turbine cycle. PGCs are a type of combustion in which there is an increase in total pressure in the combustor [2,3]. Of all the PGCs, the two promising combustors are Rotating Detonation Combustion (RDC) and Pulse Detonation Combustion (PDC). PDC consists of one or more tubes filled with fuel oxidizer and then ignited from one end, which develops into detonation. Across

the world, several studies have been conducted for combining PGC with both PDC [4,5] and RDC [6,7] to the existing gas turbine cycles. Stathopoulos [8] also conducted a cycle analysis with PGC for thermodynamic and performance calculations. The practical use of PGC concept does, however, have technical challenges. One of the major challenges is the turbine integration into the outlet of the combustor due to its highly unsteady flow and high temperature at the PGC outlet.

Still, the increase in the thermal efficiency of the engine depends on the entry temperature of the turbine. Around the year 1950, the turbine inlet temperature was kept around 1000 K and no blade cooling was considered. Different cooling methods were implemented to the blades, and in modern engines, turbine inlet temperature of around 1700 K [9] can be achieved. In PGCs, the temperature of the exhaust flow is roughly around 1500–2500 K, which is above the material-specific permissible limits, making turbine blade cooling unavoidable. The blades must be cooled to a temperature that allows for reasonable resistance to creep, as well as thermal fatigue and oxidation. A sufficiently low blade material temperature can only be achieved by combining thermal barrier coatings, alloys that are temperature-resistant, and external and internal convective cooling. As a result, typical impingement cooling or film cooling is an vital part of the cooling strategy. The arrangement of cooling air jets in terms of impingement distance, nozzle diameter, nozzle separation, and convective cross-flow schemes has a significant influence on convective heat transfer [10,11]. The interaction between the vortex and the blade surface appears to be a driving factor in improving cooling efficiency. To apply this fundamental approach to more realistic turbine cooling configurations, experimental studies on heat transfer enhancement on a flat plate induced by forced impingement jet arrays have been carried out [12]. The turbine cooling flow efficiency and the effect of cooling air injection have been studied numerically. Gaunter [13] developed a code to calculate the turbine cooling flows and the effects of cooling air injection on the turbine isentropic efficiency. Young et al. [14,15] described the thermodynamics of turbine cooling along with the associated losses. They also described different cycle layouts for the cooling. Horlock et al. [16] described several zero-dimensional cooling modeling approaches. They also provided an alternate formula for calculating the cooling mass flow rate and thermal efficiencies. Neumann et al. [17] studied pulsed impingement cooling for gas turbines and described their influence on thermal efficiency. Gao et al. [18] conducted experiments with several injection hole configurations such as compound, axial, cylindrical, and laid-back hole; they also used pressure sensitivity paint to capture the effectiveness of film cooling. They experimentally inferred that axial angled laid-back fan-shaped holes were able to distribute the coolant air uniformly and widely across the surface of the blade. Wilhelm et al. [19] studied film cooling at the rotor tip of the axial turbine. The film cooling effectiveness was determined with the pressure sensitivity paint. The researchers concluded that there exists a saturation point beyond which the cooling effectiveness remains unaffected when the cooling air mass flow is increased and also the film cooling effectiveness decreases with swirling inflows.

The turbine blade cooling air requirement has a higher impact on the turbine isentropic efficiency. As the PGC is the combustor used in this work, there is a slight increase in the combustor outlet pressure when compared with the exit of the compressor pressure. Therefore, for the initial blade row of the turbine, the cooling air requires more compression, which leads to an additional compressor. Moreover, the working fluid must be expanded over a higher pressure ratio, thus making the turbine isentropic efficiencies even more important. This can be achieved by having a secondary compressor that further compresses the cooling air to a pressure higher than the pressure of the PGC exhaust. The different cycle layouts are described in the later section of the paper.

In this work, as stated before, an unsteady 1D Euler solver is used for turbine simulations. Although 3D CFD modeling has proven useful in researching PGC-Turbine integration over the years, the unsteady nature of the PGC exhaust flow increases computational cost and time. To overcome this complexity, the reduced-order model is used instead. As an unsteady method, 1D Euler methodology is given high importance as it provides

a fast and reliable way to assess the performance of turbomachinery coupled with PGC. Asli et al. [20,21] studied the turbine interaction with PDC using the 1D unsteady Euler model and the coupled mean line analysis. The unsteady 1D Euler solver showed a good agreement when compared with unsteady 3D CFD, implying the use of a 1D solver for further turbine analysis with low computation effort. One of the unique aspects of this paper is to implement the cooling of turbine blades in the 1D unsteady Euler model and compare it with the 0D turbine blade cooling model and the unsteady 3D CFD model. For these simulations, the boundary conditions are provided by the existing in-house PDC unsteady 1D Euler model [20]. To the best of the authors' knowledge, this paper is the first to use film cooling in the unsteady 1D Euler turbine model.

## 2. Materials and Methods

The current paper focuses on the axial turbine blade cooling coupled with PDC tubes. The methodology incorporates the simulation of PDC tubes, their connection to the plenum at the exit, and the turbine module. The turbine uses an unsteady inviscid 1D Euler model with appropriate source terms, which are computed using the mean line approach. The pulsed detonation combustor is also modeled using a similar 1D Euler solver with few modifications.

This paper applies an unsteady 1D Euler solver. The used methods are shown in Figure 1. The mean line analysis is used for generating the turbine characteristic map, blade force and work source terms which are utilized by the 1D Euler solver. The validation of the mean line analysis is performed with experimental results. The PDC tubes are simulated using the in-house PDC Euler solver. Then, the unsteady boundary condition at the turbine inlet is provided by the PDC model. For the 0D models, the averaged boundary condition from the PDC model is used, and for 1D and 3D unsteady simulations, the PDC outlet boundary condition is used. In the following sections, each model is detailed. Finally, the turbine is simulated using the 0D method, the 1D Euler model and 3D CFD.

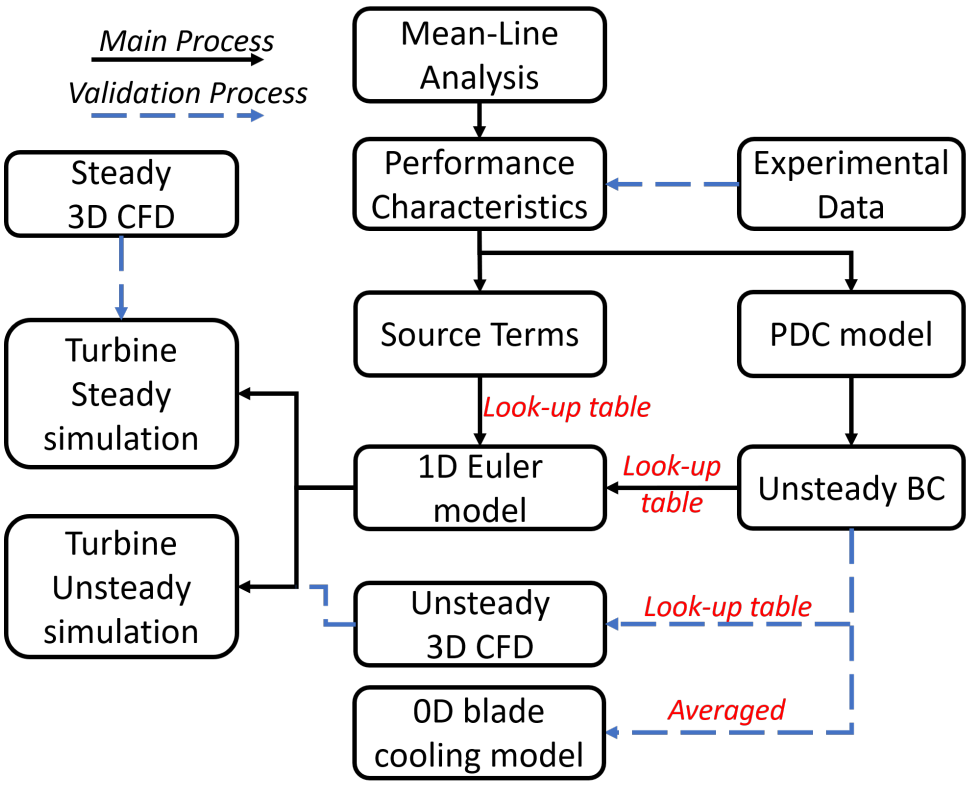


**Figure 1.** Flow chart depicting the integration and comparison of different models.

### 2.1. Axial Turbine Reference Case

The Energy-Efficient Engine's ($E^3$) high-pressure turbine [22] is used for the present activity because of the full availability of the geometry of two cooled stages whose performance is studied in terms of mean values between blade rows [22]. A summary of the aerodynamic parameters for the baseline configuration is listed in Table 1.

**Table 1.** NASA $E^3$ HPT design point parameters.

| Parameters | Value |
|---|---|
| Reduced mass flow rate (kg$\sqrt{K}$/s-kPa) | 0.892 |
| Reduced rotational speed (rad/s $\sqrt{K}$) | 33.19 |
| Total-to-total pressure ratio | 5.010 |
| Efficiency | 0.925 |

### 2.2. Mean Line Method

Mean line analysis is a reliable methodology for steady-state performance prediction. In mean line analysis, a single streamline at the mid-span connecting the inlet and outlet represents the 3D flow field of a turbomachine.

A mean line solver is developed, which includes total pressure loss correlations from Aungier [23]. The mean line solver is provided with blade geometry such as chord, height, radius, etc. At the inlet, the total pressure and total temperature are specified, and at the outlet, static pressure is given. From these input data, the program calculates the thermodynamic properties at the inlet and outlet of the module and the corresponding velocity triangles. The model used in this paper is similar to the Ainley and Mathieson method [24] with a few changes such as using empirical relationships instead of graph values. First, the air angle and the Mach number at the outlet of the blade row are assumed. Then, the co-efficient of the total pressure loss is evaluated. Finally, the exit flow parameters such as pressure, temperature, and velocity of the module are calculated. The convergence criteria are shown in Equation (1) and are similar to [24].

$$\begin{aligned} \Delta\alpha &= \left| \frac{\alpha_{out,assumed} - \alpha_{out,actual}}{\alpha_{out,assumed}} \right| < 0.1\% \\ \Delta M &= \left| \frac{M_{out,assumed} - M_{out,actual}}{M_{out,assumed}} \right| < 0.1\% \end{aligned} \tag{1}$$

If the criteria are satisfied, then the code progresses to the next blade row. If not, it assumes a different outlet air angle and outlet Mach number, and the procedure is repeated until the convergence criteria are satisfied. The source terms of the unsteady 1D Euler solver which are the force and work terms are computed with the mean line method. The source terms are the function of the pressure, the absolute velocity and the temperature of each blade row. Thus, predicting the flow parameters accurately is important to reduce the errors in simulating the 1D solver. The detailed procedure of mean line analysis and the turbine characteristic map generated using mean line analysis is shown in Appendix A.

### 2.3. 1D Euler Model

Various studies have been conducted for solving the unsteady Euler equations for turbomachinery components like compressors and turbines. However, what distinguishes this study from others is the novel approach to integrate film cooling into the unsteady 1D Euler solver for turbines. In this work, two additional source terms such as coolant mass flow rate and total enthalpy (generated by the coolant flow) are added in the mass and energy equations, respectively. The coolant flow parameters are evenly distributed along the mesh cell in the bladed region, and coolant hole blockage is also considered as a function of pressure.

The unsteady 1D Euler model is used in the current work. This approach was evaluated for the turbine by Asli et al. [20]. As stated before, this work is a further extension of

the turbine model which includes turbine blade cooling by adding two new source terms for coolant flow. The governing equations are described in Equation (2).

$$\frac{\partial}{\partial t}\begin{pmatrix}\rho A\\ \rho V_x A\\ \rho E A\end{pmatrix}+\frac{\partial}{\partial x}\begin{pmatrix}\rho V_x A\\ \rho V_x^2 A+PA\\ V_x A(\rho E+P)\end{pmatrix}=\frac{\partial}{\partial x}\begin{pmatrix}\dot{m}_{cl}\\ F_x+PA\\ W+\dot{m}_{cl}h_{t,cl}\end{pmatrix} \tag{2}$$

The source terms corresponding to the coolant flow are explained in Section 2.4. The blade force term represents the blades and the wall force term considers the force due to area change; these are the source terms in the momentum equation. The velocity of the coolant flow is neglected in the momentum equation. The various forces acting on the blade are shown in Figure 2b. The net force of the blade is a function of the momentum change between inlet and outlet Equation (3) .

$$\sum F_i = \Delta(\dot{m}V_x). \tag{3}$$

The net force acting on the blade is defined in Equation (4):

$$\sum F_i = F_{in} - F_{out} + F_{endwall} + F_x \tag{4}$$

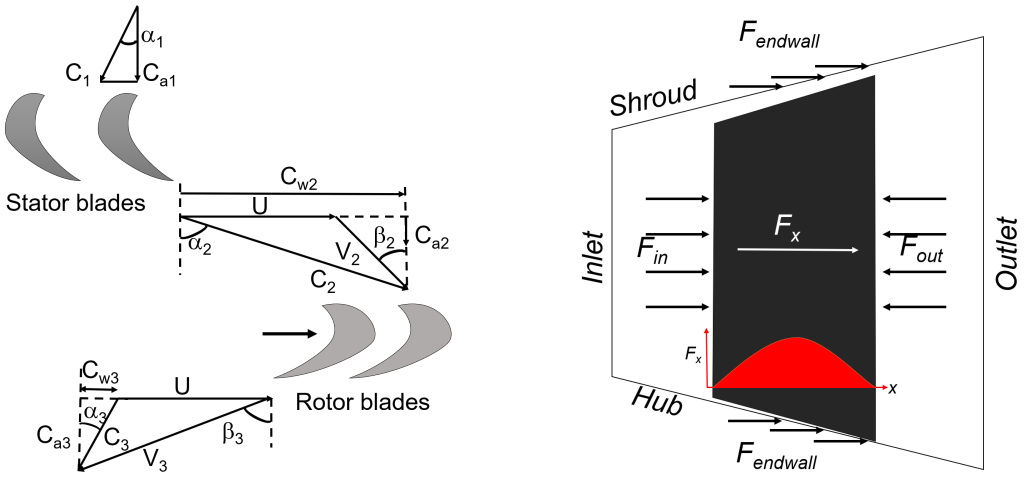


**Figure 2.** View of sample turbine blades. (**a**) Velocity triangle used in the mean line method. (**b**) Blade forces on the turbine blade.

From Equation (4), the terms $F_{in}$ and $F_{out}$ are computed by mean line analysis. The end-wall force due to the area change is solved within the solver. Combining Equations (3) and (4) and solving for $F_x$, Equation (5) is obtained, in which $F_{in} = P_{in}A_{in}$ and $F_{out} = P_{out}A_{out}$.

$$F_x = -F_{in} + F_{out} - F_{endwall} + \Delta(\dot{m}V_x) \tag{5}$$

In the energy equation, the work term considers the shaft work of the rotor blades as the source term. The shaft work is calculated using Equation (6).

$$W = (\dot{m}h_t)_{out} - (\dot{m}h_t)_{in} \tag{6}$$

The mean line method generates source terms for several operating conditions depending on the inlet boundary condition from the combustor. A look-up table is generated with the following parameters: axial location, area and mean radius of all blade rows, force source term of all blade rows, work source term of all rotor blades, static pressure, axial velocity, static temperature at entry and exit of all blade rows, rotational speed and inlet

total temperature. Depending on the inlet and exit pressure of the blade, the 1D Euler solver interpolates the respective data from the look-up table. A parabolic distribution for the source term is selected to increase numerical stability as shown in Figure 2b. The inlet boundary condition is the time-dependent total temperature and pressure from the PDC model and the outlet boundary is fixed with a static pressure of 3.63 bar. The mesh size of $\Delta x = 0.5$ mm is chosen for the domain, which is the same as in [20], for which the validation of the unsteady Euler solver was conducted by comparing it with unsteady 3D CFD. As the length of the domain is $L = 0.36$ m, the entire domain is divided into 721 cells.

### *2.4. Turbine Blade Cooling Methodology in 1D Euler Solver*

To include cooling flow effects in 1D unsteady methodology, certain assumptions are considered:

1. The cooling air enters the domain with a negligible velocity and there is no disruption to the main flow due to the coolant. Therefore, no formation of wakes or the boundary layer and also no change in the momentum are taken into account [25].
2. The coolant mass flow is evenly distributed along the computational cells including the blade. The Euler solver is aware of the location of the bladed regions and the non-bladed regions as the axial locations of the blades are specified.

The schematic diagram of cooling in a turbine blade used in the 1D model is shown in Figure 3. In this work, no cooling flows are taken into account in the non-bladed regions.

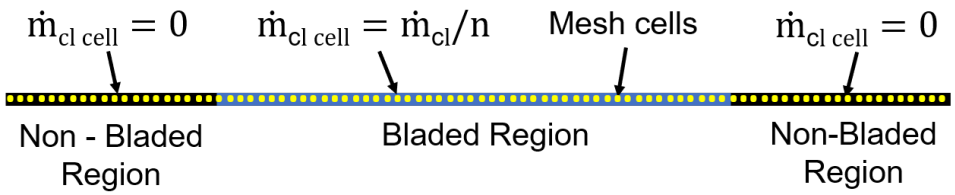


**Figure 3.** Schematic diagram of a cooled turbine blade in the 1D Euler solver.

To model the turbine blade cooling, three coolant parameters need to be specified:

1. The coolant mass flow rate, $\dot{m}_{cl}$. From Figure 3, we could see that the coolant mass flow is evenly distributed along each cell of the blade. For example, the stator-1 blade has 72 cells for which the cooling air mass flow rate is 1.5 kg/s; then, the coolant mass flow at each cell is 0.0208 kg/s.
2. The coolant temperature $T_{cl}$. It is needed for the calculation of the energy source term, $h_{t,cl}$, which is given by Equation (7).

$$h_{t,cl} = (c_{p,m}T_m - c_{p,cl}T_{cl}) + \frac{C^2}{2} \tag{7}$$

3. The coolant pressure $P_{t,cl}$. It is needed for the bleed blockage effect, that is, the coolant enters the domain when the pressure of the cooling air is higher than the pressure of the main flow at the corresponding region. The bleed blockage condition is given by Equation (8).

$$\dot{m}_{cl,cell} = \begin{cases} 0 & \text{if } P_{t,cl} < P_{t,m} \\ \frac{\dot{m}_{cl}}{n} & \text{if } P_{t,cl} > P_{t,m} \end{cases} \tag{8}$$

4. As the cooling air is introduced into the main flow, we need to consider the mixing losses. The mixing loss coefficient is given by Hartsel [26].

$$Y_{mixing} = \frac{\dot{m}_{cl}\gamma M_m^2}{2\dot{m}_m}\left[1 + \frac{T_{cl}}{T_m} - 2\frac{C_{cl}}{C_m}cos\phi\right] \tag{9}$$

As the coolant flow enters at several location around the blade, Equation (9) has to be integrated along the profile. The equation was integrated and simplified by Horlock [16], and Equation (9) became

$$Y_{mixing} = 0.07\frac{\dot{m}_{cl}}{\dot{m}_m} \tag{10}$$

The mixing loss, along with other turbine losses, is incorporated to the mean line method.

### 2.5. Cycle Layout

In this paper, two gas turbine cycle layouts with PGCs are discussed. The first cycle, shown in Figure 4a, is similar to the Joule cycle. When this layout is used, the issue arises for the turbine blade cooling. As the compressor (C1) provides the cooling air for the turbine (T1), the pressure of the coolant is lower than the pressure of the combustor exit at least for some time during the period of the combustion chamber exhaust gases, since the pressure is expected to increase through the PGC. For this case, the leading edge of the first blade row cannot be cooled down due to the bleed blockage as mentioned in Equation (8). To solve the issue, a secondary compressor (C2) can be added, which further compresses the air from the primary compressor (C1) a little more than the exhaust of the PGC, depicted in Figure 4b. The cooling air for the initial blade row of the turbine can be used from the secondary compressor to ensure no bleed blockage occurs. Also, the air from the secondary compressor can be used for PGC cooling and also as the dilution air in the ejector, if needed. For the later stages of the turbine, the coolant can be bled from the primary compressor. Also, for the whole cycle simulation [8], Layout 2 showed better performance than Layout 1.

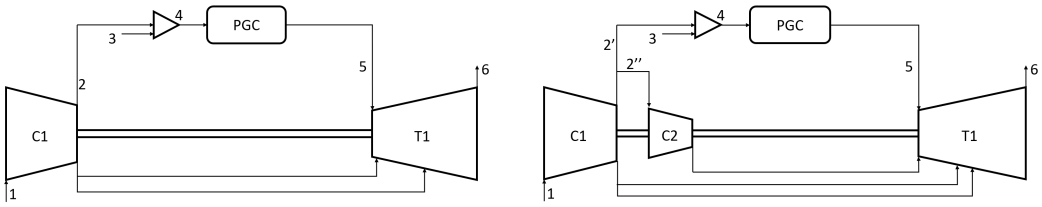


**Figure 4.** Different cycle layout types. (**a**) Layout 1. (**b**) Layout 2.

### 2.6. Pulsed Detonation Combustor Model

The PDC model is simulated with the in-house 1D solver. The equation used for the modeling of PDC tubes is shown in Equation (11). The 1D PDC tube modeling and the configuration are explained in detail by Asli et al. [20].

$$\frac{\partial}{\partial t}\begin{pmatrix}\rho\\ \rho V_x\\ \rho E\\ \rho w_{sp}\end{pmatrix} + \frac{\partial}{\partial x}\begin{pmatrix}\rho V_x\\ \rho V_x^2 + P\\ V_x(\rho E + P)\\ \rho V_x w_{sp}\end{pmatrix} = \begin{pmatrix}0\\ 0\\ 0\\ \rho \dot{w}_{sp,chem}\end{pmatrix} \tag{11}$$

As chemical composition changes, a new equation is added for each species mass fraction $w_{sp}$. The only source term in the PDC model is $\dot{w}_{sp,chem}$, which takes into account the change in chemical composition for the $H_2$–air mixture [27]. For the turbine simulations, a five-tube PDC configuration is used. The PDC–turbine integration is shown in Figure 5. The individual PDC tubes are of 1 m length and operate at 20 Hz, giving the turbine plenum an overall frequency of 100 Hz as it is a five-PDC-tube configuration.

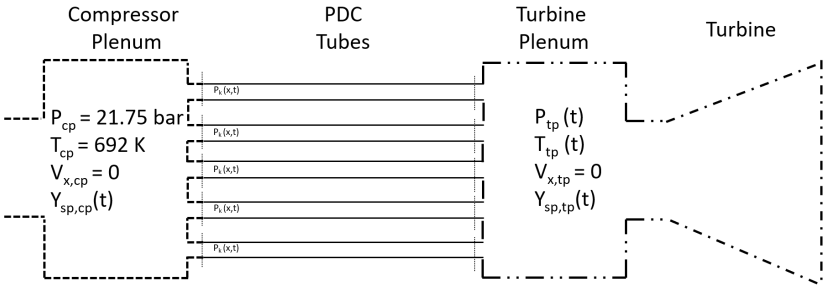


**Figure 5.** PDC setup.

### *2.7. 0D Blade Cooling Methodology*

Film cooling [28] is performed as

$$W^{+} = \frac{\epsilon_o - \epsilon_f(1-\eta_c) - \epsilon_o\epsilon_f\eta_c}{\eta_c(1-\epsilon_o)} \tag{12}$$

where the overall cooling effectiveness, $\epsilon_o$, is given a constant,

$$\epsilon_o = \frac{T_{g,in} - T_b}{T_{g,in} - T_{cl,in}} \tag{13}$$

With $W^{+}$, we can calculate the cooling air to main mass flow rate ratio $\xi$ for the blade row,

$$\xi = \frac{\dot{m}_{cl}}{\dot{m}_{g,in}} = KW^{+} \tag{14}$$

The film cooling effectiveness, $\epsilon_f$, cooling efficiency $\eta_c$ and the cooling flow factor, $K$, can be taken as constants as shown in Table 2. The constant values are taken from [8,17].

**Table 2.** Cooling parameters for 0D models.

| Parameters | Value | Parameters | Value |
|---|---|---|---|
| $\epsilon_f$ | 0.4 | $\eta_c$ | 70% |
| K | 0.045 | $T_b$ | 1100 K |

With the calculation of coolant mass flow and the temperature difference ratio, the total temperature difference can be evaluated using the energy equation [26] as shown in Equation (15).

$$\begin{aligned} \dot{m}_{g,in}h_{t,g,in} + \dot{m}_{cl}h_{t,cl} &= \dot{m}_{g,out}h_{t,g,out} = (\dot{m}_{in} + \dot{m}_{cl})h_{t,g,out} \\ \dot{m}_{g,in}c_{p,in}T_{t,g,in} + \dot{m}_{cl}c_{p,cl}T_{t,cl} &= (\dot{m}_{g,in} + \dot{m}_{cl})c_{p,out}T_{t,g,out} \end{aligned} \tag{15}$$

The exit stagnation temperature can be calculated using an iterative loop of Equation (15). The various values of $c_p$ are computed using the Shock and Detonational toolbox [29].

### *2.8. Pulsating Boundary Conditions from PDC*

Here, in this paper, a five-PDC-tube configuration was used. It combines a zero-dimensional compressor plenum upstream of the five PDC tubes and a zero-dimensional turbine plenum downstream to the combustor followed by a turbine model. The numerical setup is shown in Figure 5. A detailed explanation for the PDC model and the zero-dimensional plenum was explained in [20].

Figure 6 shows the inlet unsteady total pressure and total temperature for the turbine which is generated by the PDC-turbine plenum model.

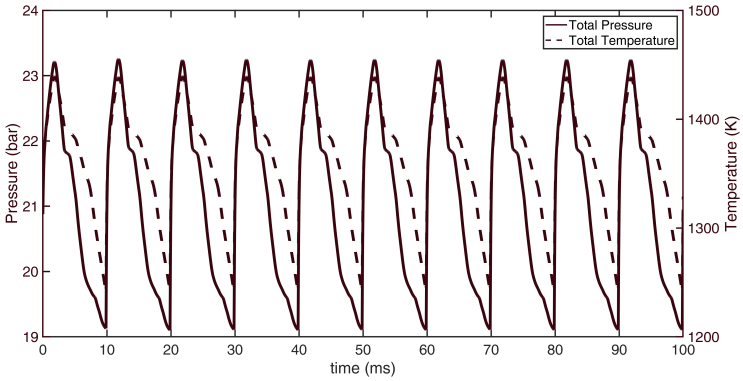


**Figure 6.** Time-dependent total pressure and total temperature in the turbine plenum.

### *2.9. Setup of the 3D CFD Simulations*

Steady and unsteady simulations of the Energy-Efficient Engine ($E^3$) two-stage configuration are performed using commercial ANSYS-CFX 2022R2 with an implicit finite volume solver. A fully second-order accurate approach is selected for the present activity. Turbulence is modeled using the $k-\omega$ SST model. All solid walls are considered adiabatic.

In steady simulations, RANS equations are evaluated considering the following boundary conditions: $P_{t,in} = 21.25$ bar, $T_{t,in} = 1350$ K, and $P_{s,out} = 3.63$ bar. To model the interface between the two blade rows, the mixing plane approach is utilized. This approach implements a circumferential average of the flow characteristic quantities. The validity of this approach is supported by the fact that fluctuations due to PDC are purely axial and that this method has been used in numerous cases similar to those in this study [30,31].

Steady-state simulation results are used as the initialization for the unsteady simulations. In the unsteady simulations, URANS equations are solved. The time discretization is implicit, using a second-order inverted Euler scheme. Profile transformation [32] is chosen to simulate a blade number of 1:2:1:2 without geometric scaling. This approach allows for simulating a non-uniform number of blades by imposing periodic boundary conditions and scaling the solutions at the interface, thus introducing an approximation as large as the difference between the pitches. This methodology is similar to the [33] domain scaling approach but has the advantage of not changing the geometries.

The unsteady simulation uses the input boundary conditions of the unsteady 1D Euler model of a pulsed detonation combustor; see Figure 6. The static output pressure is the same as in the steady-state simulations: $P_{s,out} = 3.63$ bar. The time step chosen for the unsteady simulations is $6.025 \cdot 10^{-6}$ s, in line with the time step dependency analysis conducted by Asli et al. [20]. It represents $1/10^{th}$ of the time step between the first blade and the first vane. To reach unsteady convergence, 100 periods are simulated, of which 10 are used to calculate flow statistics for comparison. A complete overview of the performed simulations is reported in Table 3.

The computational domain mesh is the same as that described by Asli [20], where a grid sensitivity study is shown considering four meshes with grids varying from 122 k to 3000 k nodes to verify the degree of dependence of the solution with respect to the number of elements. The Grid Convergence Index (GCI) values for the domain with 1132 k grids are 0.15% for pressure ratio and 0.2% for mass flow rate, respectively, which indicates that the mesh size of 1132 k nodes can be used and no further mesh refinement is needed.

Vane cooling is modeled through the use of mass source terms placed on the vane surface, thus reproducing the logic of the 1D Euler approach. The source terms involve the introduction of an additional term in the continuity equation representing the flow of the coolant within the vane control volume, as given in Equation (16).

$$\partial\rho/\partial t + \partial(\rho u_j)/\partial t = S_M \tag{16}$$

**Table 3.** 3D CFD test matrix.

| Simulation | Time Step | Cooled Vane | Boundary Condition |
|---|---|---|---|
| Steady | - | No | Steady<br>$P_{t,in}/P_{s,out} = 5.854$<br>$T_{t,in} = 1350$ K |
| Steady | - | Source term<br>$\dot{m}_{cl} = 1.5$ kg/s<br>$T_{t,cl} = 600$ K | Steady<br>$P_{t,in}/P_{s,out} = 5.854$<br>$T_{t,in} = 1350$ K |
| Unsteady | $6.025 \times 10^{-6}$ s | No | Steady<br>$P_{t,in}/P_{s,out} = 5.854$<br>$T_{t,in} = 1350$ K |
| Unsteady | $6.025 \times 10^{-6}$ s | Source term<br>$\dot{m}_{cl} = 1.5$ kg/s<br>$T_{t,cl} = 600$ K | Steady<br>$P_{t,in}/P_{s,out} = 5.854$<br>$T_{t,in} = 1350$ K |
| Unsteady | $6.025 \times 10^{-6}$ s | Source term<br>$\dot{m}_{cl} = 1.5$ kg/s<br>$T_{t,cl} = 600$ K | Pulsed [20]<br>(see Section 2.8) |

The physical values specified for each source term are the mass flow rate, the temperature of the coolant flow, and three velocity components. First, simulations with steady inlet boundary conditions are conducted to retrieve time-averaged mass-weighted total temperature values at the interfaces that are compared with results from the 0D and the 1D Euler models. Then, simulations with pulsating boundary conditions are carried out to evaluate the impact of combustor/turbine coupling and validate the unsteady 1D Euler solver. Therefore, no direct comparison with the available $E^3$ experimental data is possible. However, the aim of the activity is to demonstrate that the reduced model is able to provide results in line with 3D CFD, which is treated as a reference case.

## 3. Results

### *3.1. Steady-State Simulation*

Coolant at Stator 1

Figure 7a shows the mass flow variation of the steady 1D Euler solver and steady 3D CFD. Figure 7b offers the total temperature variations determined by the 0D model, the steady 1D Euler solver and the steady 3D CFD. According to the results, the mass flow rate across the stator remains constant and the stagnation temperature across the stator is also constant for the case without cooling, showing that the blades are adiabatic.

In the steady-state simulation, cooling is considered for the first stator. The boundary conditions for the steady-state simulation are the same as those specified for 3D CFD. The parameters used for the cooling are $\dot{m}_{cl,v1} = 1.5$ kg/s, $T_{cl,v1} = 600$ K, $P_{t,cl,v1} = 23$ bar. By using the same parameter for the coolant flow, the exit total temperature by the 0D cooling method is calculated using Equation (15).

The mass flow rate is increased due to the addition of the coolant mass flow and the stagnation temperature is decreased across the stator blade row as the blades are no longer adiabatic as a result of turbine cooling. The total temperature variation along the turbine is shown in Figure 7b. A difference of less than 2 K is seen between 0D and 1D Euler models and around 1.5 K difference between the 1D Euler model and the 3D CFD model; see Table 4. Another remarkable point on Figure 7a is that the turbine mass flow reduces slightly at the inlet of the domain when the cooling air is added for both 1D and 3D simulations. This reduction in mass flow rate is due to the turbine being constrained at both inlet and outlet with respective boundary conditions. Thus, by adding the cooling air inside the domain, both the 1D Euler solver and the 3D CFD compromise the inlet mass flow rate.

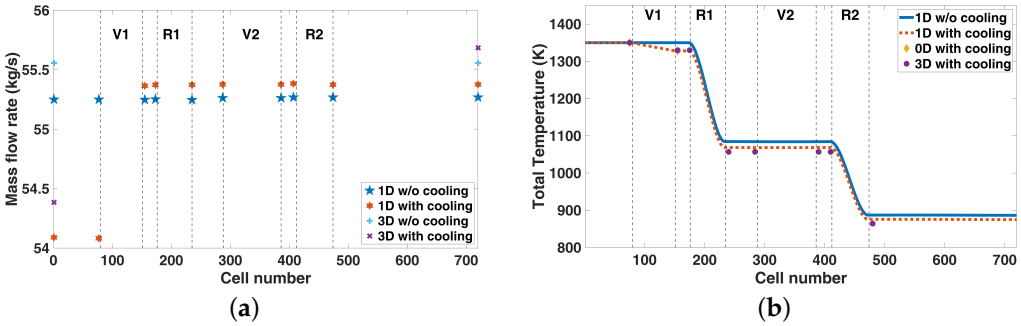


(**a**) (**b**)

**Figure 7.** Results of steady-state simulation. (**a**) Mass flow rate variation along the turbine with cooling air at Stator 1 using the steady 1D Euler solver and the steady 3D CFD. (**b**) Total temperature variation along the turbine with cooling air at Stator 1 using the steady 1D Euler solver, the 0D model and the steady 3D CFD.

### *3.2. Unsteady Simulation*

#### 3.2.1. Cooling at Stator 1

The unsteady simulation uses the boundary condition from the unsteady 1D Euler Pulsed Detonation Combustor model. The time-dependent inlet stagnation pressure and temperature are given to the unsteady 1D Euler turbine model and the source terms for various operating points are put in a look-up table and fed to the solver. For the 0D cooling model, the averaged inlet boundary conditions are used. The parameters used for the cooling are $\dot{m}_{cl,v1} = 1.5$ kg/s and $T_{cl,v1} = 600$ K, the same as in the steady-state simulation.

When the cooling flow is added, the stagnation temperature Figure 8b and the mass flow rate in Figure 8a are no longer constant and behave the same as those of steady-state simulation. The total temperature difference across Stator 1 for steady and unsteady simulation for all models is tabulated in Table 4. We can see from Table 4 that there is a small stagnation temperature difference between the models. The 0D model shows the highest difference due to its simplified approach without considering any losses by solving only the energy conservation equation as seen in Equation (15). In the 1D Euler solver, the mixing loss and two new source terms in mass and energy equations are added, but it is assumed that the cooling air enters with negligible velocity and no formation of wakes or no change in the axial momentum. The results from the 1D model are between those of the 0D and 3D models. For the 3D CFD, the cooling air is distributed in various locations on the pressure and suction side of the blade row. The stagnation temperature difference is lower for the 3D model when compared with those of 0D and 1D models because it considers the three-dimensional effect of the turbine and its losses. In general, the higher the order of simulation, the greater the accuracy due to the detailed modeling, and this trend can be seen in Table 4.

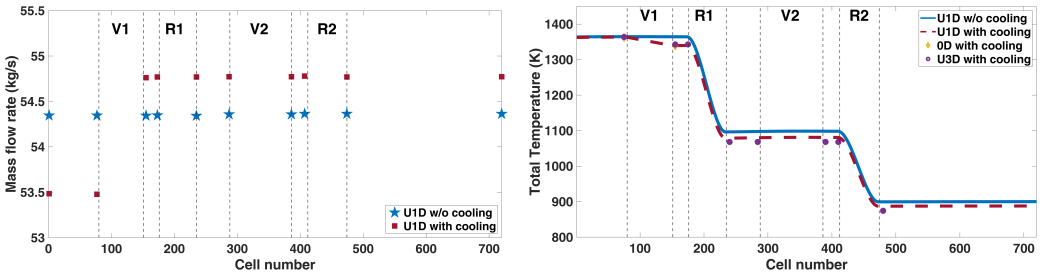


(**a**) (**b**)

**Figure 8.** Unsteady-state simulation results. (**a**) Mass flow rate variation along the turbine with cooling air at Stator 1 using the unsteady 1D Euler solver. (**b**) Total temperature variation along the turbine with cooling air at Stator 1 using the unsteady 1D Euler solver, the 0D model and the steady 3D CFD.

**Table 4.** Total temperature difference across Stator 1 with film cooling.

| Simulation | 0D | 1D | 3D |
|---|---|---|---|
| Steady | 22.90 K | 21.62 K | 20.49 K |
| Unsteady | 23.72 K | 22.76 K | 21.22 K |

3.2.2. Effect of Pulsating Conditions on Vane and Blade Loads and Overall Cycle Efficiency

Following the validation of the 1D code, 3D CFD simulations are used to quantify the impact of the pulsed conditions of inlet total temperature and pressure on the blade load of NASA $E^3$ HPT. Non-dimensional static pressure distributions for the four blades at a 50% span are reported in Figures 9 and 10. For each time step, static pressure values are normalized with the highest pressure value (occurring at the stagnation point) for the corresponding stator/rotor and time step. That procedure allows for discussing the obtained results as if isentropic Mach number distributions are showed for each time step. The orange region corresponds to the envelope of the load curves over a periodicity, while the black line represents the time-averaged static pressure distribution. Local values of pressure along the surfaces can vary considerably, thus modifying local flow velocity and ultimately blade load. That is particularly true on rotors that suffer by the fluctuation of boundary conditions more than stators.

The first stator is only impacted on the suction side, where non-negligible variations of pressure are found. However, that outcome suggests that a film cooling system designed for steady inflow conditions may work properly also in a pulsating case, at least from an aerodynamic point of view. The two rotors show higher variability and the local Mach number is highly time-dependent, thus generating harmful conditions that may impact the residual lifetime of the component. The second vane appears to have greater variability than the first one, but the fluctuations are much lower than those associated with rotors, and a major problem associated with a negative incidence is found. This problem is not caused by the pulsating conditions but by the different expansion ratio used with respect to the nominal one of the machine, coherently with 1D Euler calculations.

In this section, the turbine vane cooling effect on cycle efficiency is also provided. The use of advanced blade cooling technologies and innovative materials capable of withstanding high temperatures from the combustor has become vital. In the case of this paper, the presence of the PDC enhances that necessity since the turbine is subject to a pulsating flow with high turbine inlet temperatures. In the baseline (steady) configuration, this high-pressure vane is cooled by using 1.5 kg/s of air tapped by the compressor that is sufficient to achieve the desired film coverage of the vanes [22]. However, it must be considered that the presence of cooling implies a drop in the value of cycle efficiency. Wilcock et al. [34] evaluated this impact by proposing a formulation that quantifies the difference in cycle efficiency $\Delta\eta$ between the uncooled and cooled cases. This formulation considers the difference between the work required to compress the coolant versus that obtained from its expansion after mixing with the main flow while not considering the pressure losses in the combustor and the dissipation of kinetic energy during the mixing process between the coolant and the main flow. However, it can be considered a reliable estimation of the drop in efficiency caused by the presence of the coolant. In the present case, a $\Delta\eta$ value of 1.6% is evaluated based on the mixing pressure obtained from 3D simulations, thus taking into consideration pulsating boundary conditions. This outcome is in line with Wilcock et al. [34].

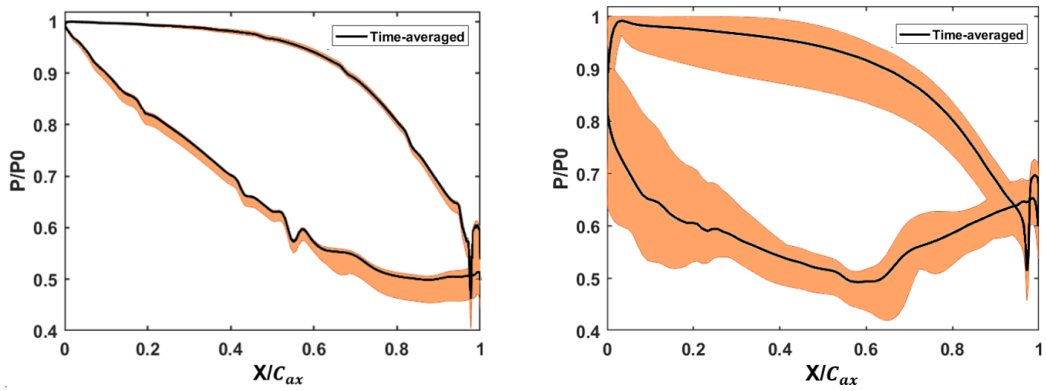


**Figure 9.** Distribution of static pressure of the first stage at mid-span using 3D CFD. (**a**) Static pressure distribution for V1 at mid-span. (**b**) R1 static pressure distribution at mid-span.

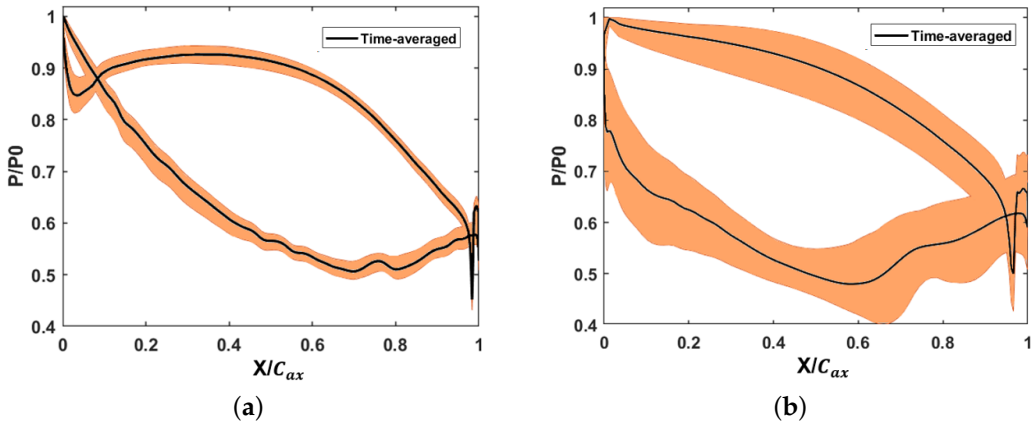


**Figure 10.** Distribution of static pressure of the second stage at mid-span using 3D CFD. (**a**) Static pressure distribution for V2 at mid-span. (**b**) R1 static pressure distribution at mid-span.

#### 3.2.3. Effect of Bleed Blockage

The PDC tubes are connected with a NASA $E^3$ high-pressure compressor upstream. The compressor has the outlet total pressure of around 21 bar and an outlet total temperature of around 700 K which is fed as the inlet condition to PDC tubes. As the PDC tubes are pressure gain combustors, at certain time steps, the PDC exit total pressure is higher than the compressor's outlet total pressure, which leads to bleed blockage effects.

Figure 11 shows a zoomed-in view of the total temperature variation in order to demonstrate the effect of the bleed blockage which is given by Equation (8). At the beginning of the stator, the total temperature is constant even after applying the coolant flow. As mentioned before, this is due to the fact that the combustor is a pressure gain combustor, that is, the inlet total pressure to the turbine is greater than, or at least equal to, that of the exit of the compressor. For the turbine cooling, the coolant air is considered to be bled from the later stage of the compressor. Thus, in certain time steps, there are some blockages in the bleed holes. In Figure 11, with the $P_{ti} = 22.7$ bar and the $P_{t,cl,v1} = 21$ bar, we can observe that the coolant flow enters the domain only when the pressure of the main flow falls below the specified cooling air pressure, which verifies the bleed blockage calculation.

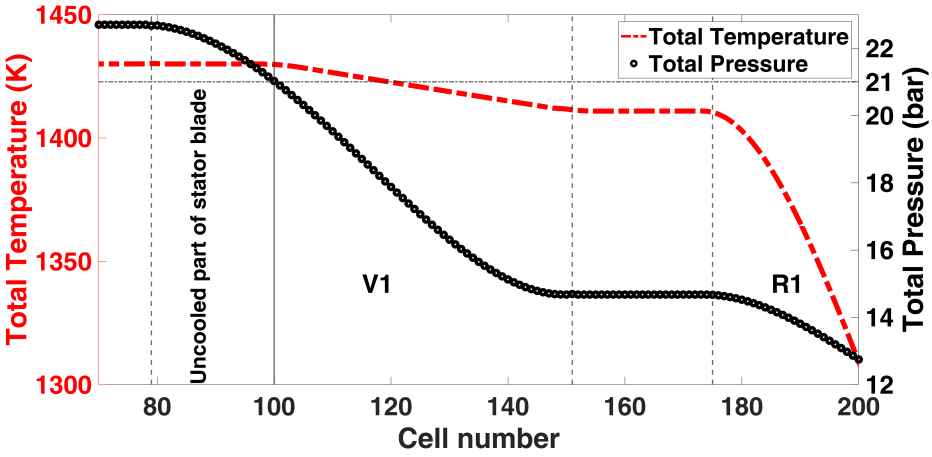


**Figure 11.** Total temperature variation along the turbine at a time step of $T_{ti} = 1430$ K, $P_{ti} = 22.7$ bar, $P_{t,cl,v1} = 21$ bar using the unsteady 1D Euler solver for Layout 1.

The main limitations of this layout are as follows: (1) as the cooling is blocked at the initial part of the blade, the leading edge of the blade is exposed to a very high temperature, probably greater than the allowable limit. This may damage the blades as the cooling is not effective there. (2) Because of the lower pressure inside the blade rows, there might be a possibility that the high pressure flow could enter into the cooling holes and rupture the blade row.

To overcome this, we consider a secondary compressor that further compresses the air from the primary compressor a little more than the PGC exhaust as shown in Figure 4b.

#### 3.2.4. Layout Comparison

For Layout 2, the coolant mass flow rate and temperature are kept constant; as for Layout 1, only the cooling air pressure is increased to $P_{t,cl,v1} = 23.5$ bar as shown in Table 5. All parts of the turbine can be cooled now as the exit pressure of the secondary compressor is higher than the inlet pressure of the turbine, which can be seen in Figure 12a. From the figure, the difference between the two layouts can be seen. A small additional secondary compressor after the primary compressor proves effective for the turbine blade cooling, providing continuous cooling air flow to the blade which can keep the blade temperature below the maximum allowable limits. In Figure 12b, we can see a higher mass flow rate at the exit of Stator 1 for Layout 2 when compared with Layout 1. This higher mass flow rate at the exit indicates that the full coolant mass flow is utilized and there is no presence of bleed blockage for Layout 2. Also, for the whole cycle simulation [8], Layout 2 shows better performance than Layout 1.

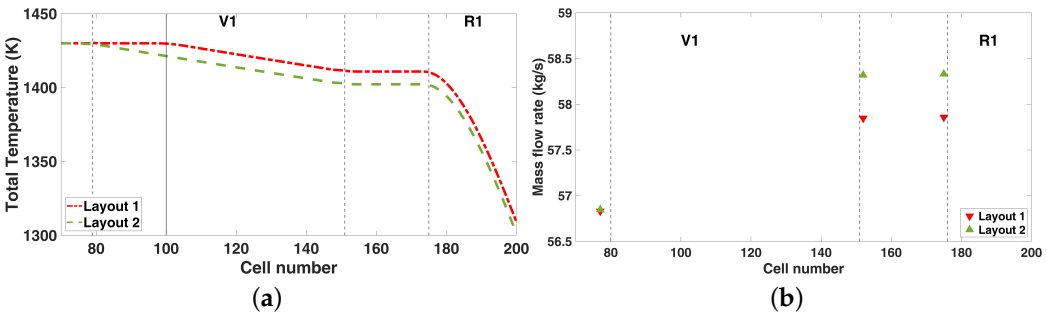


**Figure 12.** Layout comparison. (**a**) Total temperature variation along the turbine comparing two layouts at a time step of $T_{ti} = 1430$ K, $P_{ti} = 22.7$ bar using the unsteady 1D Euler solver. (**b**) Mass flow rate variation along the turbine comparing two layouts at a time step of $T_{ti} = 1430$ K, $P_{ti} = 22.7$ bar using the unsteady 1D Euler solver.

**Table 5.** Coolant parameters for layout comparison.

| Parameters | Layout 1 | Layout 2 |
|---|---|---|
| $\dot{m}_{cl,v1}$ (kg/s) | 1.5 | 1.5 |
| $T_{cl,v1}$ (K) | 700 | 700 |
| $P_{t,cl,v1}$ (bar) | 21 | 23.5 |

#### 3.2.5. Cooling for All Blade Rows

In this section, the cooling of all four blade rows is evaluated using Layout 2. The cooling flow parameters are given in Table 6. All these values are taken arbitrarily as the second compressor has not been modeled yet.

**Table 6.** Cooling flow parameters for Layout 2.

| Parameters | V1 | R1 | V2 | R2 |
|---|---|---|---|---|
| $\dot{m}_{cl}$ (kg/s) | 1.5 | 1.5 | 1 | 1 |
| $T_{cl}$ (K) | 700 | 700 | 600 | 600 |
| $P_{t,cl}$ (bar) | 23.5 | 15.5 | 10.5 | 7.5 |

Figure 13a shows the mass flow rate variation along the turbine without and with cooling using Layout 2. As observed before, we can see that there is an increase in the mass flow rate across the blade rows, indicating the additional cooling air mass flow rate. The reduction in total temperature when the cooling flow is considered is depicted in Figure 13b. We can see a decrease across the stator rows indicating that the blades are no longer adiabatic. Almost 75 K of total temperature reduction can be seen when the cooling is considered for all blade rows.

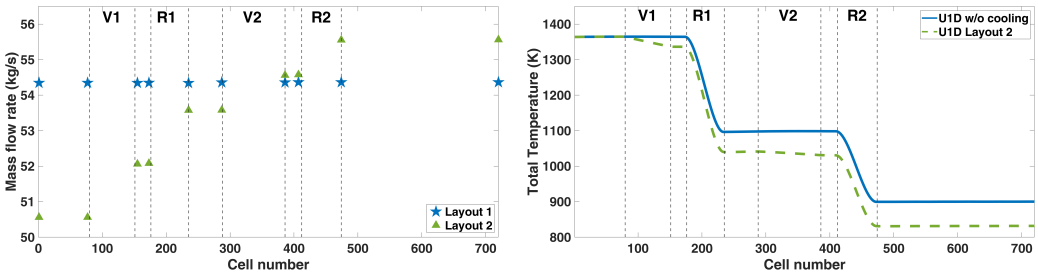


(**a**) (**b**)

**Figure 13.** Cooling of all blade rows. (**a**) Mass flow rate variation along the cooled turbine using the unsteady 1D Euler solver. (**b**) Total temperature variation along the cooled turbine using the unsteady 1D Euler solver.

## 4. Conclusions

The integration of a PGC turbine leads to high turbine inlet temperature exceeding the material limits. The main motive of this work was to incorporate the film cooling in the unsteady 1D Euler solver and validate the result with high-fidelity simulations. From the comparison plots between 0D and 3D, the 1D Euler solver showed a great match for both steady and unsteady simulations.

Although the unsteady 1D Euler solver is not a new topic to discover, a unique approach to integrate the film cooling for the turbine blades was evaluated in the existing unsteady 1D Euler model and validated with high-fidelity simulation. In the case of unsteady 1D Euler simulation, the turbine blade cooling was considered by adding two new source terms, the cooling air mass flow rate in the mass equation and the total enthalpy due to cooling air in the energy equation. The implementation of coolant mass flow, coolant temperature, and bleed blockage was discussed in detail. For the 3D CFD, the turbine

blade cooling was simulated using ANSYS CFX, where the source terms were modeled and the coolant mass flow rate, the coolant temperature, and three velocity components were specified. Using the 0D approach, film cooling was examined, the cooling air mass flow rate was obtained, and the total exit temperature calculations were performed. The film cooling results of different approaches were compared, showing a very good match. The mass flow rate variation of the uncooled turbine remained constant, and for the cooled turbine, we were able to see an increase in the overall mass flow rate due to the addition of the cooling flow. Also, as the turbine was constrained at both inlet and exit, by adding the coolant flow inside the domain, both 1D Euler and 3D CFD compromised the inlet mass flow rate. The total temperature comparison showed a less than 2 K difference between the 1D and 3D models for both steady and unsteady simulations. Concerning the 3D CFD, the obtained results allowed for validating the 1D model and shed some light on the effect of pulsating conditions on the blade load of the NASA $E^3$ HPT designed for a steady inflow, thus hinting at possible high-cycle fatigue problems generated by highly fluctuating loads.

In this work, a modified overall gas turbine layout with a secondary compressor was discussed. A small additional compressor can be added after the primary compressor, which compresses the air further than that of the PGC's exhaust pressure. The advantage of this layout over the conventional one is preventing the coolant flow blockage. In addition, an estimation of the overall cycle efficiency penalty, due to turbine vane cooling, under pulsating boundary conditions was carried out.

**Author Contributions:** Conceptualization, G.R.V.P., M.A., S.S. and P.S.; methodology, G.R.V.P. and M.A.; software, G.R.V.P., M.A., T.N. and S.S.; validation, G.R.V.P. and T.N.; formal analysis, G.R.V.P.; investigation, G.R.V.P. and T.N.; resources, G.R.V.P., M.A., T.N. and S.S.; data curation, G.R.V.P. and T.N.; writing—original draft preparation, G.R.V.P.; writing—review and editing, G.R.V.P., M.A., S.S., T.N. and P.S.; visualization, G.R.V.P., M.A., T.N. and S.S.; supervision, S.S., D.A.M. and P.S.; project administration, S.S., D.A.M. and P.S.; funding acquisition, S.S., D.A.M. and P.S. All authors have read and agreed to the published version of the manuscript.

**Funding:** This project has received funding from the European Union's Horizon 2020 research and innovation programme under the Marie Skłodowska-Curie grant agreement No 956803.

**Data Availability Statement:** Data are contained within the article.

**Acknowledgments:** The authors acknowledge Panagiotis Gallis for the useful discussions and assistance with the 3D CFD.

**Conflicts of Interest:** The authors declare no conflict of interest.

## Nomenclature

| | |
|---|---|
| $A$ | Area |
| $C$ | Absolute velocity |
| $C_{ax}$ | Axial chord |
| $c_p$ | Specific heat at constant pressure |
| $E$ | Internal energy |
| $F$ | Force |
| $h$ | Enthalpy |
| $M$ | Mach number |
| $n$ | Number of mesh cells |
| $P$ | Pressure |
| $T$ | Temperature |
| $V$ | Velocity |
| $W$ | Shaft work |
| $w_{sp}$ | Species mass fraction |
| $W^+$ | Temperature difference fraction |
| $Y$ | Total pressure loss coefficient |

| | |
|---|---|
| *Greek Symbols* | |
| $\alpha$ | Air angle |
| $\phi$ | Cooling air injection angle |
| $\xi$ | Cooling air ratio |
| $\epsilon$ | Cooling effectiveness |
| $\rho$ | Density |
| $\eta$ | Efficiency |
| $\dot{m}$ | Mass flow rate |
| $\gamma$ | Specific heat ratio |
| *Abbreviations* | |
| CFD | Computational Fluid Dynamics |
| $E^3$ | Energy-Efficient Engine |
| HPT | High Pressure Turbine |
| MLA | Mean Line Analysis |
| PGC | Pressure Gain Combustion |
| PDC | Pulsed Detonation Combustor |
| RANS | Reynolds Averaged Navier Stokes |
| RDC | Rotating Detonation Combustor |
| U1D | Unsteady One-Dimensional |
| U3D | Unsteady Three-Dimensional |
| *Subscripts* | |
| $b$ | Blade |
| $cl$ | Cooling flow |
| $c$ | Cooling |
| $f$ | Film cooling |
| $g$ | Gas |
| $in$ | Inlet |
| $m$ | Main flow |
| $o$ | Overall |
| $out$ | Outlet |
| $R1$ | Rotor 1 |
| $R2$ | Rotor 2 |
| $t$ | Total quantities |
| $s$ | Static quantities |
| $V1$ | Stator 1 |
| $V2$ | Stator 2 |
| $x$ | Axial direction |

## Appendix A. Mean line Analysis Procedure

The flow chart of the mean line analysis is shown in Figure A1. The total pressure loss correlations used for the mean line analysis are obtained from Aungier [23], which includes various losses like profile, tip clearance, secondary, shock, trailing edge, friction and mixing loss. The procedure for the mean line analysis is similar with that of the Ainley and Mathieson method [24], but correlations were used instead of the graphical values. For the mean line analysis, (1) the boundary conditions at the inlet were specified such as stagnation temperature, the corrected mass flow rate, the reduced rotational speed, the exit static pressure along with the geometrical data of each blade rows. (2) If there are no guide vanes, the inlet air angle is set of zero, the inlet Mach number is calculated using the inlet mass flow rate, as well as pressure, temperature, area and other inlet flow parameters. (3) The exit air angle ($\alpha_{out,a}$) and the exit Mach number ($M_{out,a}$) are assumed. (4) For the stator, as there is no cooling, is considered in the mean line analysis; the inlet and the outlet total temperature are the same. (5) With the geometrical data, ithe nlet flow parameters, the coefficient of the total pressure loss is evaluated. (6) With non-dimensional mass flow rate and pressure loss coefficient, the exit total pressure can be calculated. (7) As the mass flow rate is constant throughout, the exit axial velocity can be determined using the relationship between the exit mass flow rate, the exit area and density. (8) Exit absolute

velocity of the stator row can be determined using exit axial velocity and exit air angle. (9) Exit static temperature functions as an aspect of outlet stagnation temperature and outlet absolute velocity. (10) With isentropic relations, the outlet static pressure and the outlet Mach number are calculated. (11) As the Mach number at the outlet is calculated, the outlet air angle can be calculated depending on whether is flow is subsonic or supersonic. (12) Finally, the convergence is checked as in Equation (1). (13) Once the criteria are satisfied, the relative parameters are calculated from absolute parameters or vice versa, depending on the stator or rotor blade rows. (14) Then, with the exit parameter of the blade row, the next blade row is calculated using the same procedure.

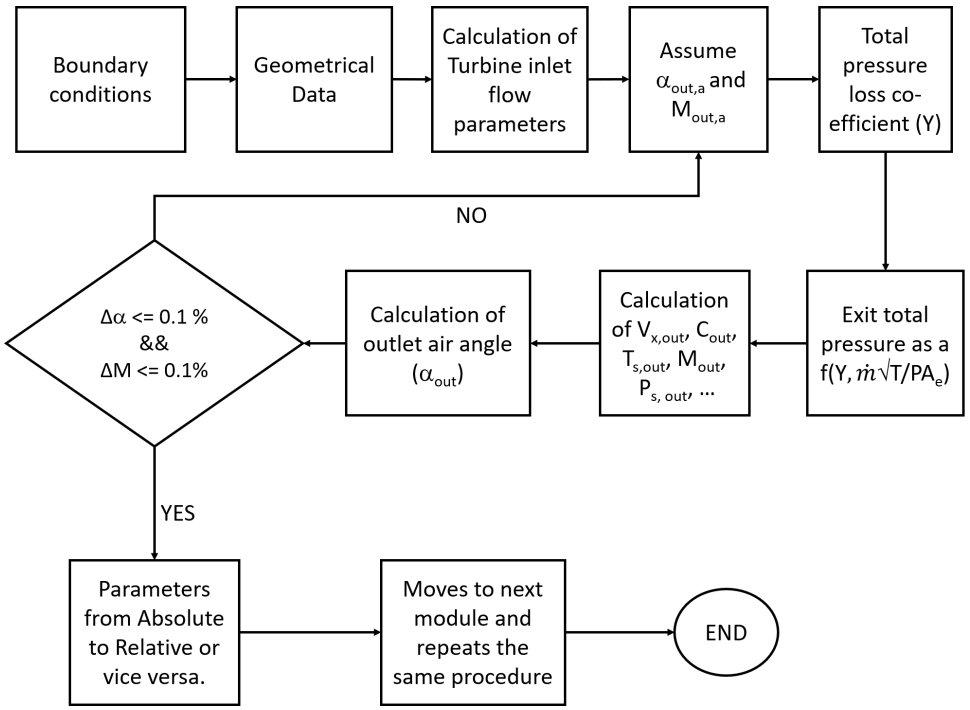


**Figure A1.** Mean line analysis flow chart.

The turbine characteristic generated from the mean line analysis for three different corrected rotational speed is shown in Figure A2.

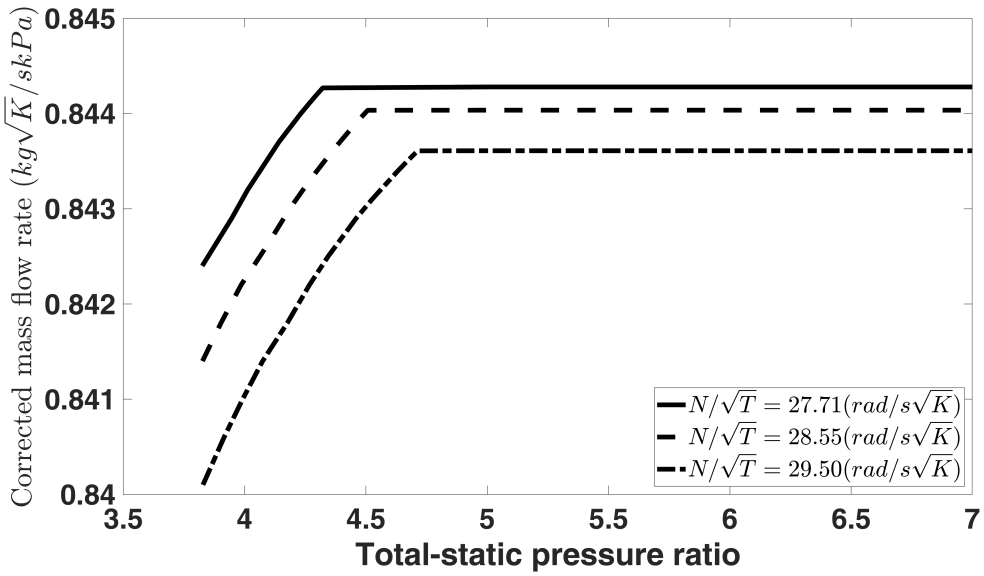


**Figure A2.** Turbine characteristic map from mean line analysis.

## References


1. International Air Transport Association. Annual Review. 2018. Available online: https://www.iata.org/contentassets/c81222d96c9a4e0bb4ff6ced0126f0bb/iata-annual-review-2018.pdf (accessed on 1 December 2021).
2. Bach, E. Performance analysis of a rotating detonation combustor based on stagnation pressure measurements. *Combust. Flame* **2020**, *217*, 21–36.
3. Kaemming, T.A.; Paxson, D.E. Determining the Pressure Gain of Pressure Gain Combustion. In Proceedings of the 2018 Joint Propulsion Conference, Cincinnati, OH, USA, 9–11 July 2018.
4. Sakurai, T.; Nakamura, S. Performance and Operating Characteristics of Micro Gas Turbine Driven by Pulse, Pressure Gain Combustor. In Proceedings of the ASME Turbo Expo 2020: Turbomachinery Technical Conference and Exposition, Virtual, Online, 21–25 September 2020.
5. Xisto, C. The efficiency of a pulsed detonation combustor—Axial turbine integration. *Aerosp. Sci. Technol.* **2018**, *82–83*, 80–91.
6. Tellefsen, J.R. Build Up and Operation of an Axial Turbine Driven by a Rotary Detonation Engine. Master's Thesis, Air Force Institute of Technology, Dayton, OH, USA, 2012.
7. Wolanski, P. Application of the Continuous Rotating Detonation to Gas Turbine. *Appl. Mech. Mater.* **2015**, *782*, 3–12.
8. Stathopoulos, P. An alternative architecture of the Humphrey cycle and the effect of fuel type on its efficiency. *Energy Sci. Eng.* **2020**, *8*, 3702–3716.
9. Sumanta, A.; Kanani, Y. Advances in Film Cooling Heat Transfer. *Adv. Heat Transf.* **2017**, *49*, 91–156.
10. Weigand, B. Multiple Jet Impingement—A Review. *Heat Transf. Res.* **2011**, *42*, 101–142.
11. Xing, J. Experimental and Numerical Investigation of Heat Transfer Characteristics of Inline and Staggered Arrays of Impinging Jets. *J. Heat Transf.* **2010**, *132*, 092201.
12. Berthold, A. Experimental Investigation of Dynamically Forced Impingement Cooling. In Proceedings of the ASME Turbo Expo, Charlotte, NC, USA, 26–30 June 2017.
13. Gaunter, J.W. *Algorithm for Calculating Turbine Cooling Flow and the Resulting Decrease in Turbine Efficiency*; NASA Technical Memorandum No. 81453; NASA: Washington, DC, USA, 1980.
14. Young, J. Modelling the Air-Cooled Gas Turbine Part 1—General Thermodynamics. *ASME J. Turbomach.* **2002**, *124*, 207–213.
15. Young, J. Modelling the Air-Cooled Gas Turbine Part 2—Coolant Flows and Losses. *ASME J. Turbomach.* **2002**, *124*, 214–221.
16. Horlock, J.H.; Watson, D.T.; Jones, T.V. Limitations on Gas Turbine Performance Imposed by Large Turbine Cooling Flows. *J. Eng. Gas Turbines Power* **2001**, *123*, 487–494.
17. Neumann, N. Pulsed Impingement Turbine Cooling and Its Effects on the Efficiency of Gas Turbines with Pressure Gain Combustion. *ASME J. Turbomach.* **2021**, *143*, 071016.
18. Gao, Z.; Narzary, D.P.; Han, J.C. Film cooling on a gas turbine blade pressure side or suction side with axial shaped holes. *Int. J. Heat Mass Transf.* **2008**, *51*, 2139–2152.
19. Wilhelm, M.; Schiffer, H.P. Experimental Investigation of Rotor Tip Film Cooling at an Axial Turbine with Swirling Inflow using Pressure Sensitive Paint. *Int. J. Turbomach. Propuls. Power* **2019**, *4*, 23.
20. Asli, M.; Garan, N.; Neumann, N.; Stathopoulos, P. A robust one-dimensional approach for the performance evaluation of turbines driven by pulsed detonation combustion. *Energy Convers. Manag.* **2021**, *248*, 114784.
21. Asli, M.; Stathopoulos, P. An Optimization Methodology for Turbines Driven by Pulsed Detonation Combustors. *J. Eng. Gas Turbines Power* **2022**, *144*, 111004.
22. Timko, L.P. *Energy Efficient Engine High Pressure Turbine Component Test Performance Report*; Technical Report NASA Contract Report; NASA: Washington, DC, USA, 1984.
23. Aungier, R.H. *Turbine Aerodynamics: Axial-Flow And Radial-Inflow Turbine Design And Analysis*; ASME Press: New York, NY, USA, 2005.
24. Ainley, D.G.; Mathieson, G.C.R. A method of performance estimation for axial-flow turbines. *Aeronaut. Res. Counc. Rep. Memo* **1951**, *2974*, 1–30.
25. Barnes, J.F.; Came, P.M. Some Aerodynamic Aspects of Turbine Blade Cooling. In Proceedings of the ASME 1969 Gas Turbine Conference and Products Show, Cleveland, OH, USA, 9–13 March 1969; V001T01A015.
26. Hartsel, J. Prediction of effects of mass-transfer cooling on the blade-row efficiency of turbine airfoils. In Proceedings of the 10th Aerospace Sciences Meeting, San Diego, CA, USA, 17–19 January 1972.
27. Burke, M.P.; Chaos, M.; Ju, Y.; Dryer, F.L.; Klippwnarwin, S.J. Comprehensive $H_2/O_2$ kinetic model for high-pressure combustion. *Int. J. Chem. Kinet.* **2012**, *44*, 444–474.
28. Holland, M.J.; Thake, T.F. Rotor blade cooling in high pressure turbines. *J. Aircr.* **1980**, *17*, 412–418.
29. Browne, S.T.; Shepherd, J.E. *SDToolbox—Numerical Tools for Shock and Detonation Wave Modeling, Explosion Dynamics Laboratory*; GALCIT Report FM2018.001; California Institute of Technology: Pasadena, CA, USA, 2021.
30. Dittmar, L.; Stathopoulos, P. Numerical Analysis of the Stability and Operation of an Axial Compressor Connected to an Array of Pulsed Detonation Combustors. In Proceedings of the ASME Turbo Expo 2020: Turbomachinery Technical Conference and Exposition, Online, 21–25 September 2020.
31. Liu, Z.; Braun, J.; Paniagua, G. Characterization of a Supersonic Turbine Downstream of a Rotating Detonation Combustor. *J. Eng. Gas Turbines Power* **2019**, *141*, 1536–1539.

32. Connell, S.; Braaten, M.; Zori, L.; Steed, R.; Hutchinson, B.; Cox, G. A comparison of advanced numerical techniques to model transient flow in turbomachinery blade rows. In Proceedings of the ASME 2011 Turbo Expo: Turbine Technical Conference and Exposition, Vancouver, BC, Canada, 6–10 June 2011.
33. Arnone, A.; Pacciani, R. Rotor-stator interaction analysis using the Navier—Stokes equations and a multigrid method. *J. Turbomach.* **1996**, *118*, 679–689.
34. Wilcock, R.C.; Young, J.B.; Horlock, J.H. The Effect of Turbine Blade Cooling on the Cycle Efficiency of Gas Turbine Power Cycles. *J. Eng. Gas Turbines Power* **2005**, *127*, 109–120.